

Article

Impacts of Crystal Quality on Carrier Recombination and Spin Dynamics in (110)-Oriented GaAs/AlGaAs Multiple Quantum Wells at Room Temperature

Satoshi Iba ^{1,*}, Ryogo Okamoto ², Koki Obu ², Yuma Obata ² and Yuzo Ohno ^{1,2} 

¹ Research Center for Emerging Computing Technologies, National Institute of Advanced Industrial Science and Technology (AIST), Tsukuba 305-8568, Japan; ono.yuzo.gb@u.tsukuba.ac.jp

² Graduate School of Pure and Applied Sciences, University of Tsukuba, Tsukuba 305-8573, Japan; ogoyrokamoto@gmail.com (R.O.); kusataipu38@yahoo.co.jp (K.O.); imperial.vortex7@gmail.com (Y.O.)

* Correspondence: s.iba@aist.go.jp

Abstract: We have systematically investigated the structural properties, carrier lifetimes, namely, photoluminescence (PL) lifetimes (τ_{PL}), and electron spin relaxation times (τ_s) in (110) GaAs/AlGaAs multiple quantum wells (MQWs) by using time-resolved PL measurements. The MQWs were grown by molecular beam epitaxy within a wide range of the growth temperature T_g (430–600 °C) and a high V/III flux ratio using As₂. At 530 °C < T_g < 580 °C, we found that the quality of the heterointerfaces is significantly improved, resulting in $\tau_{PL} \sim 40$ ns at RT, one order of magnitude longer than those reported so far. Long τ_s (~6 ns) is also observed at RT.



Citation: Iba, S.; Okamoto, R.; Obu, K.; Obata, Y.; Ohno, Y. Impacts of Crystal Quality on Carrier Recombination and Spin Dynamics in (110)-Oriented GaAs/AlGaAs Multiple Quantum Wells at Room Temperature. *Micromachines* **2021**, *12*, 1112. <https://doi.org/10.3390/mi12091112>

Academic Editor: Nozomi Nishizawa

Received: 23 July 2021

Accepted: 9 September 2021

Published: 16 September 2021

Publisher's Note: MDPI stays neutral with regard to jurisdictional claims in published maps and institutional affiliations.



Copyright: © 2021 by the authors. Licensee MDPI, Basel, Switzerland. This article is an open access article distributed under the terms and conditions of the Creative Commons Attribution (CC BY) license (<https://creativecommons.org/licenses/by/4.0/>).

1. Introduction

Semiconductor spintronics has attracted growing interest in the last three decades [1]. In nonmagnetic semiconductors, the retention time of electron spin polarization, i.e., the spin relaxation time (τ_s), is one of the most important indexes because it significantly affects the performance of spintronic devices such as spin transistors [2] and spin-photonics devices [3–5]. For III-V compound semiconductors, τ_s in bulk and (100)-oriented quantum wells (QWs) have been extensively investigated so far [6,7]. In the last two decades, on the other hand, much attention has been focused on spin dynamics in non-(100)-oriented QWs, where electron spins have apparently different behaviors from those in (100) QWs [8]. As such, (110) QWs are considered to be one of several promising platforms with applications for spin-photonic devices, as well as studies of spin physics [9–13], due to long τ_s of about several nanoseconds at room temperature (RT) [14]. The key parameter to induce such a long τ_s is the Dresselhaus-type effective magnetic fields (B_{eff}) generated by spin-orbit interaction via the inversion asymmetry of crystal structure in zincblende III-V compound semiconductors. The direction and the magnitude of B_{eff} depend on the electron wavevector, and this allows us to control the arrangement of B_{eff} by changing the direction of quantum confinement of electron wavefunctions. In (100) QWs, which are widely used in conventional electronic and photonic devices, B_{eff} are in in-plane directions for all the in-plane wavevectors. This results in the random precession of electron spins initially aligned to the out-of-plane directions, and the fast relaxation of the ensemble of electron spins. This process is called the D'yakonov–Perel (DP) spin relaxation mechanism [7]. In contrast with (100) QWs, the distribution of B_{eff} in wavevector space for (110) QWs is uniaxial anisotropy oriented in out-of-plane direction. This leads to the suppression of the spin precession for electron spins aligned to out-of-plane direction [15]. Therefore, the out-of-plane B_{eff} induced by the Dresselhaus spin-orbit coupling provides τ_s in the order of nanoseconds at RT, which is an order of magnitude longer than that of (100) QWs [14]. Taking advantage of these excellent features, slow light propagation via coherent population oscillation [16],

long-distance spin transport [17], τ_s modulation by introducing superlattice structures [18] as well as by applying gate vias [19], and circularly polarized lasing in vertical cavity surface emitting laser by optical spin injection [20] have been demonstrated in GaAs-based (110) QWs at RT.

To develop spin-photonic devices, we should also pay attention to the lifetime of carriers at RT, i.e., photoluminescence (PL) lifetime (τ_{PL}), which is one of the indicators of the crystal quality. There are, however, only a few studies reporting τ_{PL} in undoped (110) GaAs/AlGaAs QWs, the value of which is only several nanoseconds [21–23]. This value is an order of magnitude shorter than those observed in high-quality (100) GaAs/AlGaAs QWs [24,25]. This indicates that there is room for improvement in crystal growth technology for (110) GaAs/AlGaAs QWs. To develop high-quality materials is indispensable for device applications. In crystal growth on GaAs (110) substrates, it is challenging to keep stoichiometry composition and incorporate constituent atoms in the lattice simultaneously, due to the non-polar surface of the GaAs (110) plane [26]. The deviation from stoichiometry and inadequate incorporation of adatoms, which are significantly affected by the growth temperature (T_g) in molecular beam epitaxy (MBE), can cause various crystal defects such as point defects and stacking faults. These degrade the optical properties of the epitaxial layers. To overcome the difficulties, we prepared (110) GaAs/AlGaAs QWs by MBE with varying T_g in a wide range under the irradiation of large numbers of As atoms. Systematic investigations of the structural and optical properties revealed that τ_{PL} exhibits the longest value of 40 ns at $T_g = 580$ °C, which is one order of magnitude longer than those with conventional growth conditions for GaAs (110). The longest τ_s is also obtained at 530 °C < T_g < 580 °C.

2. Experimental Methods

All the samples studied here were grown on epi-ready, semi-insulating (110) on-axis GaAs substrates by an Eiko EV-100 MBE system. Seven samples consisted of 10 nm GaAs cap layers, 60 periods of 10 nm GaAs/10 nm Al_{0.3}Ga_{0.7}As multiple quantum wells (MQWs), and 300 nm Al_{0.3}Ga_{0.7}As/100 nm GaAs buffer layers. The MQW structure was adopted to obtain sufficient PL intensity and to facilitate the time-resolved PL measurements. Prior to the growth, a native oxide on the surface was removed by heating the substrate up to 610 °C under As₂ exposure. The growth conditions used for all layers are as follows: growth rate of GaAs was 0.5 μm/h, T_g was varied from 432 to 600 °C, and beam equivalent pressure (BEP) ratio of As₂ to Ga was set at 80, measured by using a nude ion gauge. The As₂ beam was generated by using a valved cracking cell. Careful consideration of growth conditions is important for high-quality growth on GaAs (110). Epitaxial growth on (110) surfaces is known to be more difficult than that on (100) surfaces [27]. Widely used growth conditions for growth on (100) surfaces ($T_g \sim 580$ °C and BEP ratio of As₄ to Ga~10) lead to poor (110) surface morphology. It has been pointed out that the optimum growth of smooth GaAs (110) layers requires a relatively high As₄/Ga BEP ratio (40–80) and low growth temperatures (<500 °C). However, such low temperatures result in poor PL properties. Therefore, in this study, we attempted film growth with a wide range of T_g (432–600 °C) under a high BEP ratio. Here, we mention the importance of using As₂ as the arsenic species. Since both Ga and As atoms coexist on non-polar GaAs (110) surfaces, the arsenic incorporation coefficient during the growth of GaAs decreases to 50% or less of that on (100) surface when As₄ is used [26]. With the use of As₂, on the other hand, the incorporation coefficient is improved about twice as much as in the case of As₄ [26]. It should be noted that the detection sensitivity of the nude ion gauge is different between As₂ and As₄. In our experiments, the cracking temperature was raised from 600 to 900 °C to change the main arsenic species from As₄ to As₂. Then, while the temperature of the As source was fixed, the As beam flux detected by the nude ion gauge decreased to one-fifth. Therefore, the number of As atoms for the BEP ratio of As₂/Ga = 80 corresponded to five times as much as As₄/Ga = 80. It will be shown in the next section that the irradiation of

such a large number of As atoms is important for preventing As deficiency on the growth surface to conduct stoichiometric film growth.

For structural analysis, we carried out reflection high-energy electron diffraction (RHEED), atomic force microscopy (AFM), X-ray diffraction (XRD), and transmission electron microscope (TEM) measurements. To evaluate static optical and structural properties, continuous wave (CW) PL measurements were conducted. Carrier and spin dynamics were characterized by time-resolved PL (TRPL) measurements. In the CW-PL measurements, samples were excited by a diode-pumped solid-state (DPSS) laser. The laser wavelength was 532 nm (2.331 eV), which can excite not only GaAs well layers but also Al_{0.3}Ga_{0.7}As barrier layers whose band gap energy is 1.802 eV at 300 K. The spot size was about 100 μm diameter, and the intensity was 0.5 mW. In the TRPL measurements, samples were excited by right circularly polarized pump pulses generated by a picosecond wavelength-tunable, mode-locked Ti:Al₂O₃ laser. The diameter of the laser spot was about 60 μm . The laser's average intensity was 1 mW. The excitation wavelength was set at about 70 nm shorter than that of the PL peak, which means that electron–hole pairs are excited only within the QW region.

To evaluate τ_{PL} and τ_s , the TRPL measurements were carried out. In the measurements, spin-polarized electrons—which were excited to the state of the conduction band by right circularly polarized ($\sigma+$) excitation pulses through the spin-dependent optical selection rules—radiatively decayed to the state of the valence band. The resulting PL was partially circularly polarized, reflecting the degree of spin polarization of the recombination electrons. Right-($I_{\sigma+}(t)$) and left-($I_{\sigma-}(t)$) circularly polarized components of the PL were separately converted to orthogonal linearly polarized light by using a quarter-wave plate and a linear polarizer. The PLs were finally measured by using a streak camera through a 25 cm monochromator. As a typical result, the TRPL data for the sample with $T_g = 432^\circ\text{C}$ are shown in Figure 1. τ_{PL} is given by fitting $I_{\sigma+}(t) + I_{\sigma-}(t)$ with a single exponential decay function $\sim \exp(-t/\tau_{\text{PL}})$. From the calculated temporal circular polarization (P_c) of the PLs, $P_c(t) = (I_{\sigma+} - I_{\sigma-})/(I_{\sigma+} + I_{\sigma-})$, we obtained τ_s by using a fitting function defined as $P_c(t) \sim \exp(-2t/\tau_s)$ [28]. Here, we should note that the hole spins are practically unpolarized, due to their short spin relaxation times [29]. The circular polarization observed for the PL therefore comes from the spin polarization of electrons in the conduction band.

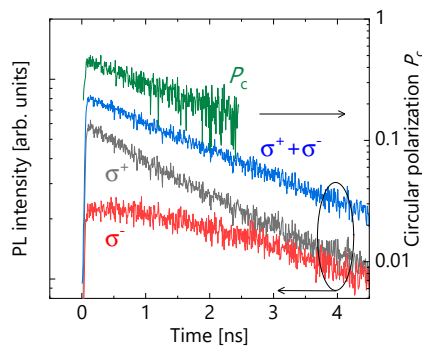


Figure 1. Typical results of polarization- and time-resolved photoluminescence (PL) decay signal for the sample grown at growth temperatures (T_g) of 432°C measured at room temperature (RT). Circular polarization (P_c) is given by $(I_{\sigma+} - I_{\sigma-})/(I_{\sigma+} + I_{\sigma-})$, where $I_{\sigma+}$ and $I_{\sigma-}$ represent right- and left-circularly polarized PL components under $\sigma+$ excitation, respectively.

3. Results and Discussions

3.1. Characterizations of Sample Structures and Static Photoluminescence

This section describes sample structure analysis and static PL properties by RHEED, AFM, XRD, CW-PL, and TEM. First, we will explain surface analysis provided by the RHEED measurements. Since the RHEED patterns did not show growth temperature dependence, as a typical result, RHEED images before and after the growth of a sample with $T_g = 580^\circ\text{C}$ are shown in Figure 2a,b. The characteristic (1×1) patterns reflecting

bulk periodicity were observed before and after growth, indicating that surface reconstruction did not occur, which is the same as the previous report [26]. Thus, the lesser amount of information obtained from the RHEED measurements on the GaAs (110) surface compared to the widely used GaAs (100) surface makes crystal growth on the GaAs (110) surface difficult.

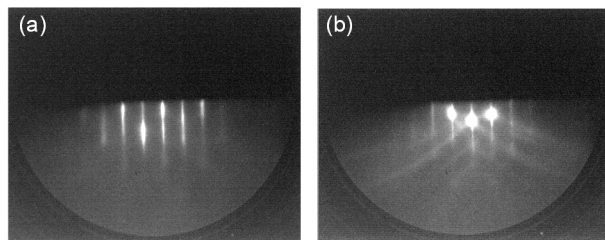


Figure 2. $[1\bar{1}0]$ azimuth RHEED patterns from (a) a GaAs (110) substrate after desorption of a native oxide, (b) a GaAs (110) cap layer on the MQW structure with $T_g = 580$ $^{\circ}\text{C}$. Both patterns indicate (1×1) non-reconstructed surface.

The surface morphology of the GaAs cap layer of the sample measured by AFM will be presented. Figure 3a,c,e,g,h are wide-area AFM images ($20 \times 20 \mu\text{m}^2$) for the samples with $T_g = 432, 476, 530, 580$, and 600 $^{\circ}\text{C}$, respectively. In the sample with $T_g = 432$ $^{\circ}\text{C}$, as shown in Figure 3a, a vertically long pattern (along the $[1\bar{1}0]$) direction) with a height of about 1 nm was observed. When T_g was raised to 530 $^{\circ}\text{C}$, the shape changed to a rounded pattern, and the height of the pattern increased to 5 nm. When T_g was raised further to 580 $^{\circ}\text{C}$, the shape changed to a triangle, and its height increased significantly to 40 nm. Tok et al. reported that such triangular patterns can be induced by the local agglomeration and clustering of Ga atoms due to As deficiency [27]. In the sample grown at 600 $^{\circ}\text{C}$, the density of the triangular pattern with a height of about 40 nm increased. The value of the average surface roughness (R_a) of each sample is shown in the figures. R_a increased with T_g , reaching about 9 nm when T_g was 600 $^{\circ}\text{C}$. Nevertheless, the surfaces were mirror-like, not clouded, which is desirable for the PL measurements. We note here that, in the previous report where As_4 was used with BEP ratio of about 80, the triangular patterns appeared at $T_g = 480$ $^{\circ}\text{C}$ [21], whereas not observed when $T_g < 580$ $^{\circ}\text{C}$ in the present study. This means that using As_2 and a high As_2/Ga BEP ratio successfully suppressed As deficiency and Ga agglomeration even at higher growth temperatures (500 $^{\circ}\text{C} < T_g < 580$ $^{\circ}\text{C}$) resulting in improvements in surface morphology. Above 580 $^{\circ}\text{C}$, on the other hand, a significant decrease in the As incorporation coefficient [26] caused As deficiency on the growth surface, forming triangular patterns. The AFM images with a narrow area ($1 \times 1 \mu\text{m}^2$) of the samples with $T_g = 432, 476$, and 530 $^{\circ}\text{C}$ are shown in Figure 3b,d,f. Step-and-terrace structures having a vertically long pattern with a height of 1–2 monolayers were observed in the sample with $T_g = 432$ $^{\circ}\text{C}$. As T_g increased, the terrace shape became isotropic, and the size increased significantly from several tens of nm to about $1\mu\text{m}$. This suggests that for low $T_g < 476$ $^{\circ}\text{C}$, the anisotropic surface diffusion of Ga atoms was induced, which obeys the difference of the migration barrier of Ga atoms between [1] and $[1\bar{1}0]$ in-plane direction [30]. On the other hand, the diffusion became isotropic due to the high thermal energy as T_g increased.

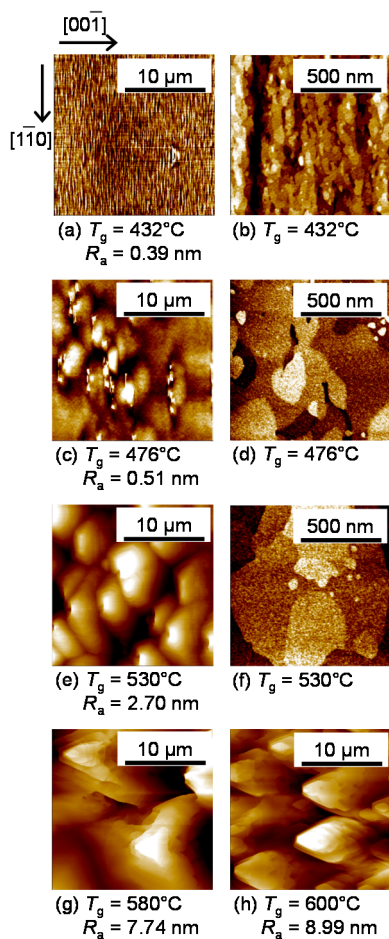


Figure 3. Atomic force microscopy (AFM) images with a scan size of $20 \times 20 \mu\text{m}^2$ in (a,c,e,g,h), and of $1 \times 1 \mu\text{m}^2$ in (b,d,f), for the surface of the samples grown at given T_g . The value of the average surface roughness (R_a) of each sample is also shown in the figures. Crystal orientation is indicated by the arrows in (a).

Next, the results of XRD measurements are discussed. The data of θ - 2θ scan at the (220) diffraction of each sample is shown in Figure 4. In all the samples, satellite peaks reflecting the periodicity of the MQW structure was detected at the same angle. This reveals that the average thickness of the GaAs wells and AlGaAs barriers are the same for all samples. However, it can be seen that the linewidths of the satellite peaks were remarkably widened, and the peak intensities were lowered in the samples with $T_g = 580$ and 600°C . This indicates that the fluctuation of the thicknesses between layers is remarkably large in these samples.

We next explain the results of the CW-PL measurements at RT. Figure 5a shows T_g dependence in the PL spectra. For all the samples, the PL peaks appeared at the same wavelength. Since the PL wavelength reflects the quantum confinement of carriers, Figure 5a indicates that the quantum structures with the same average well width are formed with different T_g . This seems to be consistent with the XRD analysis showing satellite peaks at the same angle, as shown in Figure 4. The integrated PL intensity of each sample is summarized in Figure 5b. The integrated PL intensity had a peak behavior. When T_g was raised from 432 to 580°C , the PL intensity increased about 50 times, and then for $T_g = 600^\circ\text{C}$ it decreased to about a half of that of 580°C . The PL intensity is determined by the competition between radiative and non-radiative recombination processes [31]. Therefore, the significant increase in the PL intensity suggests that the non-radiative recombination process is remarkably suppressed by increasing T_g . This interpretation will be explained in detail in the next section. Figure 5c shows PL spectra normalized by peak intensity in each spectrum. There was almost no change in the spectral shape in T_g range of

432 to 530 °C. The main peak at 851 nm corresponds to the electron-heavy hole transition, and the 843 nm sub-peak corresponds to the electron–light hole transition of their ground state. These measured PL wavelengths almost match the transition wavelengths calculated from given QW structures. The spectral linewidth began to widen at $T_g = 580$ °C. This is attributed to the variation in the transition energy, reflecting thickness fluctuations of GaAs well layers in the in-plane and stacking direction in the photoexcited region, which is similar to the T_g dependence observed by the XRD and AFM measurements.

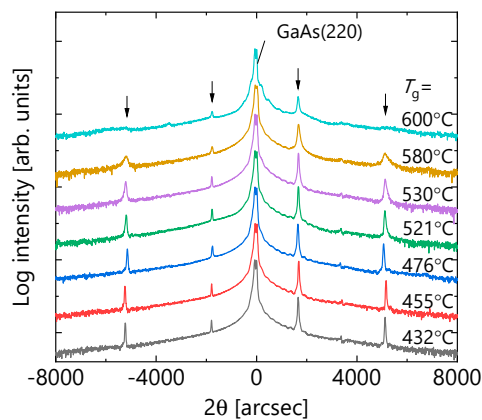


Figure 4. X-ray diffraction (XRD) profiles of θ - 2θ scan at the (220) diffraction for the samples with given T_g . The x-axis is the angle relative to the diffraction angle of GaAs. The satellite peaks derived from the periodic structure of multiple quantum wells (MQWs) are indicated by the arrows.

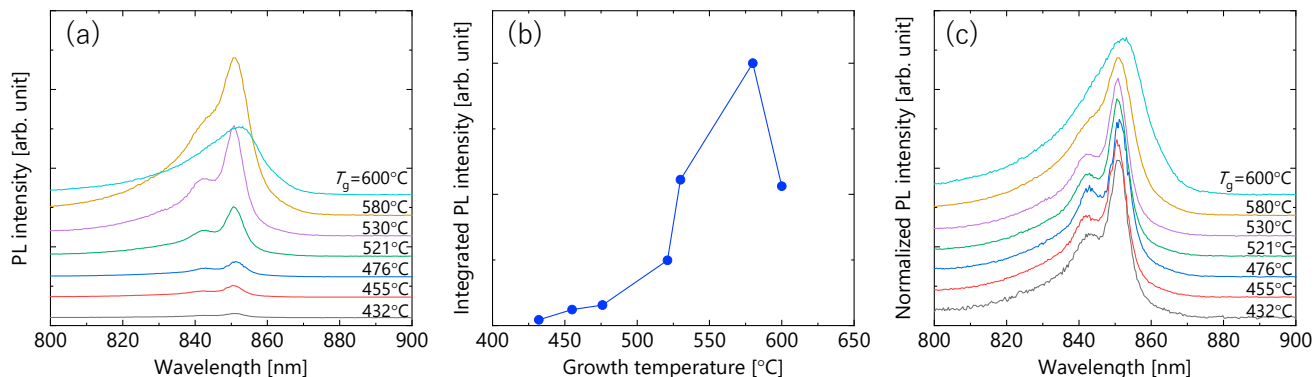


Figure 5. The data of continuous wave (CW)-PL measurements performed at RT. (a) PL spectra for the samples with given T_g , (b) integrated PL intensity plotted as a function of T_g , and (c) PL spectra normalized by the peak intensity for each spectrum depicted in (a).

To visually verify the structure fluctuations at higher T_g , cross-sectional TEM analysis was carried out for the sample grown at 600 °C. The scan area depicted in Figure 6 is beneath the apex of the triangular pattern observed in Figure 3h. Stacking faults, which can be caused by the deviations from stoichiometry [32], were formed diagonally, and the thicknesses of GaAs well and AlGaAs barrier layers fluctuated by several nm or more. Such film thickness fluctuations caused a decline in satellite peaks in XRD data in Figure 4, and an increase in the PL linewidth in Figure 5c. Since the stacking faults and point defects that exist around them can act as non-radiative recombination centers, it is reasonable that the PL intensity decreased in a 600 °C sample with many triangular patterns having stacking faults.

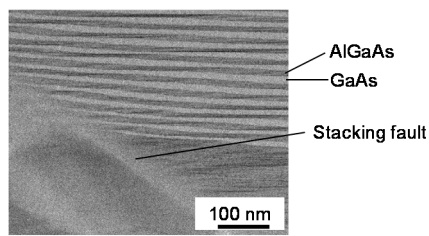


Figure 6. Cross-sectional transmission electron microscope (TEM) image for the sample grown at $T_g = 600\text{ }^\circ\text{C}$. The scan area is beneath the apex of the triangular pattern observed in Figure 3h. In the striped pattern, dark (light) gray areas represent AlGaAs (GaAs) layers. The observed stacking fault is along the $\langle 111 \rangle$ direction.

3.2. Carrier and Spin Dynamics

In this section, we investigate the carrier and spin dynamics measured by the TRPL method. Figure 7a shows the T_g dependence of τ_{PL} measured at RT. Similar to T_g dependence of CW-PL intensity (shown in Figure 5b), τ_{PL} increased with T_g monotonously up to $T_g = 580\text{ }^\circ\text{C}$, and then decreased with further increases in T_g . The maximum τ_{PL} , 40 ns, at $T_g = 580\text{ }^\circ\text{C}$ is the longest value that has been reported in (110) GaAs/AlGaAs MQWs so far, and comparable to that for high-quality (100) MQWs [24,25]. To investigate carrier dynamics in detail, we extracted the radiative recombination time (τ_R) and the non-radiative recombination time (τ_{NR}) from the temperature dependence of τ_{PL} and PL intensity (I_{PL}). τ_{PL} and I_{PL} are given by the following equations using τ_R and τ_{NR} , respectively [31].

$$\frac{1}{\tau_{PL}} = \frac{1}{\tau_R} + \frac{1}{\tau_{NR}} \quad (1)$$

$$I_{PL} = \frac{1/\tau_R}{1/\tau_R + 1/\tau_{NR}} \quad (2)$$

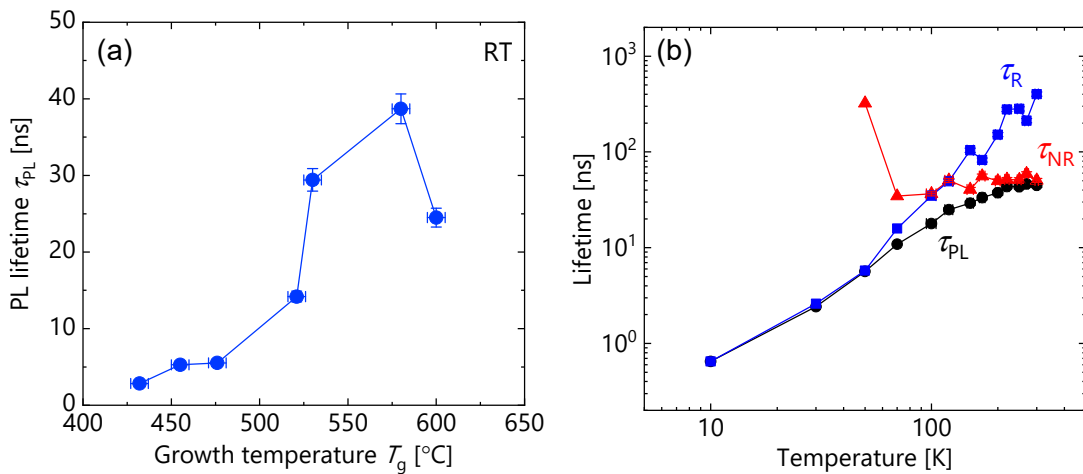


Figure 7. (a) Growth temperature dependence of PL lifetimes (τ_{PL}) measured at RT. (b) Temperature dependence of PL lifetimes (τ_{PL} ; solid circles), radiative recombination time (τ_R ; solid squares) and non-radiative recombination time (τ_{NR} ; solid triangles) for the sample grown at $T_g = 580\text{ }^\circ\text{C}$.

Figure 7b shows the temperature dependence of τ_R and τ_{NR} obtained from Equations (1) and (2), together with τ_{PL} and I_{PL} measured at each temperature for the sample with $T_g = 580\text{ }^\circ\text{C}$. It was found that τ_{NR} became shorter than τ_R above 150 K, resulting in significantly dominating τ_{PL} , namely, $\tau_{PL} \sim \tau_{NR}$. Similar behavior was observed for all the samples. Accordingly, the increase in τ_{NR} ($\sim \tau_{PL}$) at RT for a range of T_g from 432 to 580 $^\circ\text{C}$ in Figure 7a means the decrease in the density of non-radiative recombination center. In (100) GaAs/AlGaAs MQWs, it has been pointed out that the interface non-radiative recombination caused by lattice defects and incorpo-

rated impurities near the GaAs/AlGaAs interface determines the τ_{NR} at RT [24,25]. Therefore, we should consider that the increase in τ_{NR} is attributed to the suppression of interface non-radiative recombination, namely, improvements in interface quality by increasing T_g to 580 °C. The increasing tendency of terrace size in Figure 3b,d,f may support this interpretation. On the other hand, the drop in τ_{NR} (τ_{PL}) at $T_g = 600$ °C presumably originated from the non-radiative recombination centers induced by a large number of stacking faults underneath triangular patterns (see Figures 3h and 6) and point defects around the stacking faults, rather than the effect of improving the interface quality. Therefore, MBE growth of optically high-quality (110) GaAs/AlGaAs MQWs is possible by setting moderately higher T_g (>500 °C), although it has been believed that low T_g (<500 °C) is preferable for crystal growth on GaAs (110) [33].

Finally, the T_g dependence of τ_s obtained at RT by circularly polarized TRPL measurements is discussed. Figure 8 shows τ_s as a function of T_g . τ_s increased with T_g up to 476 °C, then saturated to 530 °C. The longest τ_s (>6 ns) was obtained around $T_g = 530$ °C. On the other hand, the decrease in τ_s was observed when $T_g \geq 580$ °C. As explained in the previous section, the fluctuation of the MQW structure was remarkable for samples with $T_g = 580$ and 600 °C. As can be seen from the cross-sectional TEM image of Figure 6, there were some regions where the interfaces of MQW faced non-(110) plane direction. The quantum confinement with tilting from the (110) orientation caused an in-plane component of B_{eff} induced by the Dresselhaus spin–orbit coupling. This promoted the relaxation of spins initially aligned along the out-of-plane direction [22]. This is surely the mechanism by which the τ_s decreased in high- T_g samples.

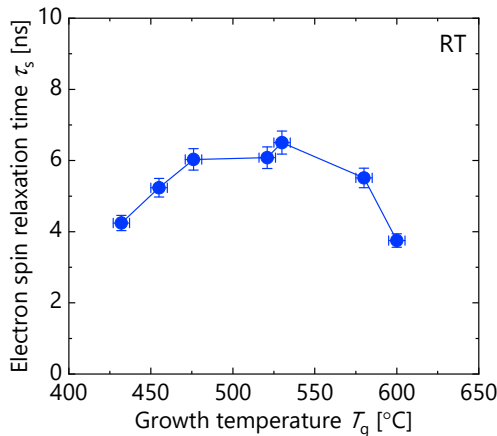


Figure 8. Growth temperature dependence of electron spin relaxation times (τ_s) measured at RT.

Here, we discuss the mechanism of increasing τ_s for $T_g \leq 476$ °C. To date, intersubband scattering mechanism [9], and Bir–Aronov–Pikus (BAP) mechanism [14,34] have been proposed for electron spin relaxation mechanisms in (110) GaAs/AlGaAs MQWs at RT. The former depends on the electron concentration and the intersubband energy gap, and the latter depends on the hole concentration. The macroscopic structures of the samples prepared here were almost the same, as shown in the XRD and CW-PL data. In addition, the excitation intensity in the TRPL measurements was the same for all samples, resulting in the same concentrations of the photoexcited electrons and holes for each our sample. Therefore, the possibility that these spin relaxation mechanisms modulate τ_s should be negligible.

One can come up with following possible scenario: interface imperfections in the (110) MQWs cause additional spin relaxation. There are two candidates for interface imperfections: an interface compositional gradient layer, and interface crystal defects including impurities. Regarding the former, Karimov et al. reported a calculation result that τ_s is reduced to 1/30 by introducing an interface compositional gradient layer with the thickness of two monolayers [35]. In contrast, it is reported that the Rashba split energy that induces in-plane B_{eff} is negligibly small for the MQW having compositional variations,

which means that τ_s is not modulated [36,37]. Since whether the compositional gradient layers are present or not is not sure in our samples, we do not mention their effects on τ_s .

Regarding the latter, the lattice defects and impurities near interfaces may induce random potential, which causes enhancement of spin relaxation by the random Rashba effect [38,39]. As discussed above, the T_g dependence of τ_{PL} at RT, which corresponds to τ_{NR} , suggests that the number of the lattice defects and impurities near the interfaces decrease when T_g increases. Therefore, it is natural that τ_s has T_g dependence. Figure 8 shows the weak T_g dependence of τ_s , compared to that of τ_{PL} . This difference originated from the fact that τ_{PL} directly reflects the lattice defects and impurities near interfaces, whereas τ_s is indirectly related to the interface quality. The DP mechanism induced by the Rashba spin–orbit coupling through the compositional gradient layers, and/or spin relaxation mechanisms other than the DP mechanism, can act dominantly in high-quality samples with moderately high T_g (middle 500 °C) as to determine the upper limit of τ_s . We also mention that even the sample with T_g of 432 °C—having the lowest interface quality among our samples—shows τ_s of about 4 ns, which is still an order of magnitude longer than that of (100) QWs. This suggests that the Rashba in-plane B_{eff} induced by interface imperfections is significantly smaller than the Dresselhaus in-plane B_{eff} in (100) QWs. Further investigation is needed for clarifying the mechanisms such as *local* Rashba spin–orbit coupling for limiting τ_s in an ideal (110) QWs without any crystal imperfections.

4. Conclusions

In order to optimize MBE growth conditions to obtain a long photoluminescence lifetime (τ_{PL}) and electron spin relaxation time (τ_s) in (110)-oriented GaAs/AlGaAs multiple quantum wells (MQWs), we systematically investigated impacts of crystal quality on carrier recombination and spin dynamics in (110) MQWs with growth temperatures in the range of 430 to 600 °C. The MBE growth of (110) MQWs at moderately high growth temperatures (middle 500 °C range) under irradiation of a large number of As atoms provides significant improvements in interface quality, resulting in long τ_{PL} (~40 ns) as well as τ_s (~6 ns) at RT. These findings obtained will be useful information in developing high-performance spintronics devices.

Author Contributions: Conceptualization, S.I. and Y.O. (Yuzo Ohno); methodology, S.I. and Y.O. (Yuzo Ohno); validation, S.I. and Y.O. (Yuzo Ohno); formal analysis, S.I. and Y.O. (Yuzo Ohno); investigation, S.I. and Y.O. (Yuzo Ohno); resources, S.I. and Y.O. (Yuzo Ohno); data curation, S.I., R.O., K.O., Y.O. (Yuma Obata) and Y.O. (Yuzo Ohno); writing original draft preparation, S.I. and Y.O. (Yuzo Ohno); writing review and editing, S.I. and Y.O. (Yuzo Ohno); visualization, S.I.; supervision, Y.O. (Yuzo Ohno); project administration, S.I. and Y.O. (Yuzo Ohno); funding acquisition, S.I. and Y.O. (Yuzo Ohno). All authors have read and agreed to the published version of the manuscript.

Funding: This work was supported by JSPS KAKENHI (Grant Number JP19H02181 and JP19K05243) and ALTA Innovative Science and Technology Initiative for Security (Grant Number JPJ004596).

Data Availability Statement: The data presented in this study are available on request from the corresponding author.

Conflicts of Interest: The authors declare no conflict of interest.

References

- Žutić, I.; Fabian, J.; Sarma, S.D. Spintronics: Fundamentals and applications. *Rev. Mod. Phys.* **2004**, *76*, 323. [[CrossRef](#)]
- Sugahara, S.; Nitta, J. Spin-transistor electronics: An overview and outlook. *Proc. IEEE* **2010**, *98*, 2124. [[CrossRef](#)]
- Holub, M.; Bhattacharya, P. Spin-polarized light-emitting diodes and lasers. *J. Phys. D Appl. Phys.* **2007**, *40*, R179. [[CrossRef](#)]
- Nishizawa, N.; Nishibayashi, K.; Munekata, H. Pure circular polarization electroluminescence at room temperature with spin-polarized light-emitting diodes. *Proc. Natl. Acad. Sci. USA* **2017**, *114*, 1783. [[CrossRef](#)]
- Žutić, I.; Xu, G.; Lindemann, M.; Junior, P.E.F.; Lee, J.; Labinac, V.; Stojšić, K.; Sipahi, G.M.; Hofmann, M.R.; Gerhardt, N.C. Spin-lasers: Spintronics beyond magnetoresistance. *Solid State Commun.* **2020**, *316*, 113949. [[CrossRef](#)]
- Meir, F.; Zakharchenya, B.P. *Optical Orientation*; Elsevier: Amsterdam, The Netherlands, 1984.
- D'yakonov, M.I. *Spin Physics in Semiconductors*; Springer: New York, NY, USA, 2008.

8. Hernández-Mínguez, A.; Biermann, K.; Hey, R.; Santos, P.V. Spin transport and spin manipulation in GaAs (110) and (111) quantum wells. *Phys. Status Solidi B* **2014**, *251*, 1736. [[CrossRef](#)]
9. Döhrmann, S.; Hägle, D.; Rudolph, J.; Bichler, M.; Schuh, D.; Oestreich, M. Anomalous spin dephasing in (110) GaAs quantum wells: Anisotropy and intersubband effects. *Phys. Rev. Lett.* **2004**, *93*, 147405. [[CrossRef](#)]
10. Bernevig, B.A.; Orenstein, J.; Zhang, S.-C. Exact SU (2) symmetry and persistent spin helix in a spin-orbit coupled system. *Phys. Rev. Lett.* **2006**, *97*, 236601. [[CrossRef](#)] [[PubMed](#)]
11. Couto, O.D.D., Jr.; Iikawa, F.; Rudolph, J.; Hey, R.; Santos, P.V. Anisotropic spin transport in (110) GaAs quantum wells. *Phys. Rev. Lett.* **2007**, *98*, 036603. [[CrossRef](#)] [[PubMed](#)]
12. Chen, Y.S.; Fält, S.; Wegscheider, W.; Salis, G. Unidirectional spin-orbit interaction and spin-helix state in a (110)-oriented GaAs/(Al, Ga) As quantum well. *Phys. Rev. B* **2014**, *90*, 121304(R). [[CrossRef](#)]
13. Völkl, R.; Schwemmer, M.; Griesbeck, M.; Tarasenko, S.A.; Schuh, D.; Wegscheider, W.; Schüller, C.; Korn, T. Spin polarization, dephasing, and photoinduced spin diffusion in (110)-grown two-dimensional electron systems. *Phys. Rev. B* **2014**, *89*, 075424. [[CrossRef](#)]
14. Ohno, Y.; Terauchi, R.; Adachi, T.; Matsukura, F.; Ohno, H. Spin relaxation in GaAs (110) quantum wells. *Phys. Rev. Lett.* **1999**, *83*, 4196. [[CrossRef](#)]
15. D'yakonov, M.I.; Kachorovskii, V.Y. Spin relaxation of two-dimensional electrons in noncentrosymmetric semiconductors. *Sov. Phys. Semicond.* **1986**, *20*, 110.
16. Palinginis, P.; Sedgwick, F.; Crankshaw, S.; Moewe, M.; Chang-Hasnain, C. Room temperature slow light in a quantum-well waveguide via coherent population oscillation. *Opt. Express* **2005**, *13*, 9909. [[CrossRef](#)] [[PubMed](#)]
17. Yokota, N.; Aoshima, Y.; Ikeda, K.; Kawaguchi, H. Room temperature spin transport in undoped (110) GaAs/AlGaAs quantum wells. *Appl. Phys. Lett.* **2014**, *104*, 072406. [[CrossRef](#)]
18. Ohno, Y.; Iba, S.; Okamoto, R.; Obata, Y.; Obu, K.; Dominguez, J.J.P.; Saito, H. Room-temperature spin relaxation in a (110)-oriented GaAs/AlGaAs superlattice with tunnel-coupled quantum wells. *Appl. Phys. Express* **2020**, *13*, 123003. [[CrossRef](#)]
19. Iba, S.; Koh, S.; Kawaguchi, H. Room temperature gate modulation of electron spin relaxation time in (110)-oriented GaAs/AlGaAs quantum wells. *Appl. Phys. Lett.* **2010**, *97*, 202102. [[CrossRef](#)]
20. Iba, S.; Koh, S.; Ikeda, K.; Kawaguchi, H. Room temperature circularly polarized lasing in an optically spin injected vertical-cavity surface-emitting laser with (110) GaAs quantum wells. *Appl. Phys. Lett.* **2011**, *98*, 081113. [[CrossRef](#)]
21. Iba, S.; Fujino, H.; Fujimoto, T.; Koh, S.; Kawaguchi, H. Correlation between electron spin relaxation time and hetero-interface roughness in (110)-oriented GaAs/AlGaAs multiple-quantum wells. *Physica E* **2009**, *41*, 870. [[CrossRef](#)]
22. Koh, S.; Nakanishi, A.; Kawaguchi, H. Electron spin relaxation time in GaAs/AlGaAs multiple quantum wells grown on slightly misoriented GaAs (110) substrates. *Appl. Phys. Lett.* **2010**, *97*, 081111. [[CrossRef](#)]
23. Iba, S.; Saito, H.; Watanabe, K.; Ohno, Y.; Yuasa, S. Systematic study of surface morphology, photoluminescence efficiency, and spin-detection sensitivity in (110)-oriented GaAs/AlGaAs quantum wells. *Jpn. J. Appl. Phys.* **2016**, *55*, 113001. [[CrossRef](#)]
24. Dawson, P.; Woodbridge, K. Effects of prelayers on minority-carrier lifetime in GaAs/AlGaAs double heterostructures grown by molecular beam epitaxy. *Appl. Phys. Lett.* **1984**, *45*, 1227. [[CrossRef](#)]
25. Foxon, C.T.; Cheng, T.S.; Dawson, P.; Lacklison, D.E.; Orton, J.W.; van der Vleuten, W.; Hughes, O.H.; Henini, M. External photoluminescence efficiency and minority carrier lifetime of (Al,Ga)As/GaAs multi-quantum-well samples grown by molecular beam epitaxy using both As₂ and As₄. *J. Vac. Sci. Technol. B* **1994**, *12*, 1026. [[CrossRef](#)]
26. Tok, E.S.; Jones, T.S.; Neave, J.H.; Zhang, J.; Joyce, B.A. Is the arsenic incorporation kinetics important when growing GaAs (001), (110), and (111) A films? *Appl. Phys. Lett.* **1997**, *71*, 3278. [[CrossRef](#)]
27. Tok, E.S.; Neave, J.H.; Ashwin, M.J.; Joyce, B.A.; Jones, T.S. Growth of Si-doped GaAs (110) thin films by molecular beam epitaxy; Si site occupation and the role of arsenic. *J. Appl. Phys.* **1998**, *83*, 4160. [[CrossRef](#)]
28. Seymour, R.J.; Alfano, R.R. Time-resolved measurement of the electron-spin relaxation kinetics in GaAs. *Appl. Phys. Lett.* **1980**, *37*, 231. [[CrossRef](#)]
29. Damen, T.C.; Via, L.; Cunningham, J.E.; Shah, J.; Sham, L.J. Subpicosecond spin relaxation dynamics of excitons and free carriers in GaAs quantum wells. *Phys. Rev. Lett.* **1991**, *67*, 3432. [[CrossRef](#)]
30. Ishii, A.; Aisaka, T.; Oh, J.-W.; Yoshita, M.; Akiyama, H. Low and anisotropic barrier energy for adatom migration on a GaAs (110) surface studied by first-principles calculations. *Appl. Phys. Lett.* **2003**, *83*, 4187. [[CrossRef](#)]
31. Gurioli, M.; Vinattieri, A.; Colocci, M.; Deparis, C.; Massies, J.; Neu, G.; Bosacchi, A.; Franchi, S. Temperature dependence of the radiative and nonradiative recombination time in GaAs/Al_xGa_{1-x}As quantum-well structures. *Phys. Rev. B* **1991**, *44*, 3115. [[CrossRef](#)]
32. Kim, H.; Yeu, I.W.; Han, G.; Ju, G.; Lee, Y.J.; Shin, Y.; Choi, J.H.; Koo, H.C.; Kim, H. Surface morphology evolution and underlying defects in homoepitaxial growth of GaAs (110). *J. Alloys Compd.* **2021**, *874*, 159848. [[CrossRef](#)]
33. Fawcett, P.N.; Neave, J.H.; Zhang, J.; Joyce, B.A. The observation of monolayer and bilayer growth during the deposition of GaAs (110) films by molecular beam epitaxy. *Surf. Sci.* **1993**, *296*, 67. [[CrossRef](#)]
34. Bir, G.L.; Aronov, A.G.; Pikus, G.E. Spin relaxation of electrons due to scattering by holes. *Zh. Eksp. Teor. Fiz.* **1975**, *69*, 1382.
35. Karimov, O.Z.; John, G.H.; Harley, R.T.; Lau, W.H.; Flatté, M.E.; Henini, M.; Airey, R. High temperature gate control of quantum well spin memory. *Phys. Rev. Lett.* **2003**, *91*, 246601. [[CrossRef](#)]

36. Eldridge, P.S.; Leyland, W.J.H.; Lagoudakis, P.G.; Harley, R.T.; Phillips, R.T.; Winkler, R.; Henini, M.; Taylor, D. Rashba spin-splitting of electrons in asymmetric quantum wells. *Phys. Rev. B* **2010**, *82*, 045317. [[CrossRef](#)]
37. English, D.J.; Hübner, J.; Eldridge, P.S.; Taylor, D.; Henini, M.; Harley, R.T.; Oestreich, M. Effect of symmetry reduction on the spin dynamics of (001)-oriented GaAs quantum wells. *Phys. Rev. B* **2013**, *87*, 075304. [[CrossRef](#)]
38. Sherman, E.Y. Random spin-orbit coupling and spin relaxation in symmetric quantum wells. *Appl. Phys. Lett.* **2003**, *82*, 209. [[CrossRef](#)]
39. Zhou, Y.; Wu, M.W. Spin relaxation due to random Rashba spin-orbit coupling in GaAs (110) quantum wells. *Europhys. Lett.* **2010**, *89*, 57001. [[CrossRef](#)]